Ion-dependent protein–surface interactions from intrinsic solvent response

Jesse L. Prelesnik[a,1], Robert G. Alberstein[b,1], Shuai Zhang[c,d], Harley Pyles[e,f], David Baker[e,f,g], Jim Pfaendtner[a,h], James J. De Yoreo[c,d], F. Akif Tezcan[b,i,2], Richard C. Remsing[j,2], and Christopher J. Mundy[h,k,2]

[a]Department of Chemistry, University of Washington, Seattle, WA 98195; [b]Department of Chemistry and Biochemistry, University of California, San Diego, La Jolla, CA 92093; [c]Physical Sciences Division, Physical and Computational Sciences Directorate, Pacific Northwest National Laboratory, Richland, WA 99354; [d]Materials Science and Engineering, University of Washington, Seattle, WA 98195; [e]Department of Biochemistry, University of Washington, Seattle, WA 98195; [f]Institute for Protein Design, University of Washington, Seattle, WA 98195; [g]HHMI, University of Washington, Seattle, WA 98195; [h]Department of Chemical Engineering, University of Washington, Seattle, WA 98195; [i]Materials Science and Engineering, University of California, San Diego, La Jolla, CA 92093; [j]Department of Chemistry and Chemical Biology, Rutgers University, Piscataway, NJ 08854; and [k]Chemical Physics Theory Team, Pacific Northwest National Laboratory, Richland, WA 99354

Edited by Peter J. Rossky, Rice University, Houston, TX, and approved May 6, 2021 (received for review December 14, 2020)

The phyllosilicate mineral muscovite mica is widely used as a surface template for the patterning of macromolecules, yet a molecular understanding of its surface chemistry under varying solution conditions, required to predict and control the self-assembly of adsorbed species, is lacking. We utilize all-atom molecular dynamics simulations in conjunction with an electrostatic analysis based in local molecular field theory that affords a clean separation of long-range and short-range electrostatics. Using water polarization response as a measure of the electric fields that arise from patterned, surface-bound ions that direct the adsorption of charged macromolecules, we apply a Landau theory of forces induced by asymmetrically polarized surfaces to compute protein–surface interactions for two muscovite-binding proteins (DHR10-mica6 and ^{C98}RhuA). Comparison of the pressure between surface and protein in high-concentration KCl and NaCl aqueous solutions reveals ion-specific differences in far-field protein–surface interactions, neatly capturing the ability of ions to modulate the surface charge of muscovite that in turn selectively attracts one binding face of each protein over all others.

soft matter | solution assembly | specific ion effects | electrostatics | Landau theory

Solid–liquid interfaces promote many phenomena that are of central importance in fields ranging from geochemistry to energy science (1, 2). Moreover, the templating interactions between mineral surfaces and biomolecules are known to have far-reaching implications in our understanding of the origins of life and the synthesis of novel functional materials (3, 4). Natural bioinorganic materials exhibit a diversity of physical properties adapted for organismal fitness (5, 6) (e.g., nacre, composed of calcium carbonate platelets interconnected by proteins and other biopolymers to provide both strength and flexibility, and collagen, which forms bone, tendon, and cartilage as a function of mineral content) that are selectively produced under controlled conditions that modulate heterogeneous self-assembly. However, our fundamental understanding of such interfaces at the molecular scale has remained limited, precluding the development of synthetic biomaterials from first principles. Much progress has been made in experimentally probing solid–solution interfaces. Surface-sensitive techniques such as X-ray reflectivity (7), second-harmonic spectroscopy (8), three-dimensional fast force mapping (9), dynamic force spectroscopy (10), and the surface force apparatus (11) continue to contribute to our understanding of how the properties of the solid surface in conjunction with the solution conditions (e.g., ionic strength, electrolyte type) impact interfacial speciation and ultimately modulate the forces between surfaces. These concepts become particularly important at the nanoscale where the length scales of molecular fluctuations near an interface become comparable to that of the solution response (e.g., screening) (12). This convergence of scales, in turn, enables processes such as oriented attachment as a new pathway for synthesis of nanocrystals, which is known to be inextricably tied to the nature of both the surface and the solution conditions (13–15). It is clear that our understanding of such interfacial phenomena requires a theoretical platform that effectively captures molecular-scale details to understand physical outcomes at the macroscopic scale.

Herein, we utilize designed proteins as a sensitive probe of the underlying solution conditions and their effect on the synthesis of materials on a solid, templating surface. The construction of synthetic biomaterials from designed, information-rich macromolecular building blocks (e.g., proteins) promises precisely tailored material properties, but is confounded by the vast parameter space underpinning their self-assembly (16, 17). Of these, materials that contain a high degree of ordering are

Significance

Hard–soft interfaces between inorganic surfaces and biomolecules promote self-assembly processes with broad implications in biogeochemistry, energy sciences, nanomedicine, and origins of life. Yet, detailed molecular-scale understanding of inorganic–biomolecule interactions and their dependence on solution conditions is missing. We present a theory for the initial stages of inorganic–biomolecule assembly based on the far-field response of water, using experimentally characterized interactions between muscovite surfaces and mica-binding proteins as model systems. Our work connects molecular details of the solution to assembly outcomes and suggests the initial driving forces for assembly are dominated by long-range, ion-specific interactions. The connections made between interfacial structure and long-range surface–biomolecule interactions provide insights toward a predictive understanding of biomolecular self-assembly on mineral surfaces.

Author contributions: J.L.P., R.G.A., J.P., F.A.T., R.C.R., and C.J.M. designed research; J.L.P., R.G.A., R.C.R., and C.J.M. performed research; S.Z., H.P., D.B., and J.J.D.Y. contributed new reagents/analytic tools; J.L.P., R.G.A., S.Z., H.P., R.C.R., and C.J.M. analyzed data; J.L.P., R.G.A., F.A.T., R.C.R., and C.J.M. wrote the paper; and D.B. and J.J.D.Y. are principal investigators.

The authors declare no competing interest.

This article is a PNAS Direct Submission.

[1]J.L.P. and R.G.A. contributed equally to this work.

[2]To whom correspondence may be addressed. Email: chris.mundy@pnnl.gov, rick.remsing@rutgers.edu, or tezcan@ucsd.edu.

This article contains supporting information online at https://www.pnas.org/lookup/suppl/doi:10.1073/pnas.2025121118/-/DCSupplemental.

Published June 25, 2021.

particularly desirable targets, as they are amenable to structure determination methods, can serve as scaffolds with well-defined spacings for functionalization with chemical groups, and possess specific physicochemical properties based on the composition (and arrangement) of the individual building units (18). Template materials with near-perfect basal cleavage are naturally well suited to the production of low-dimensional ordered materials, as they provide atomically flat crystalline surfaces with well-defined surface properties. The phyllosilicate mineral mica, particularly the *C*2/*c* symmetric pseudohexagonal muscovite, is an ideal example owing to its other desirable physical properties: It is chemically and thermally inert, insoluble, lightweight, insulating, flexible, inexpensive, and hydrophilic (19). Consequently, various nanoscale objects such as DNA have been successfully adsorbed onto the atomically flat muscovite from aqueous solution in an orientationally specific manner, an important step toward building complex structures (20, 21).

Adsorbates of particular interest are proteins, which can be de novo designed and/or mutated to modulate mica binding affinity. Recently, a designed helical repeat (DHR) protein featuring tandem repeats of helix-turn-helix subunits (22), designated DHR10-micaX (where X equals the number of repeats), was designed such that glutamate residues precisely matched the lattice spacing of the hexagonal array of potassium ions on the muscovite surface (23). This allows the rod-shaped proteins to assemble in alignment with the three principal axes of the underlying ion lattice as measured by atomic force microscopy (AFM) in a variety of solution conditions (23, 24). Interestingly, its surface coverage and uniformity in orientation are sensitive to the ionic strength of the aqueous medium, among other variables such as protein concentration and ion species (Fig. 1 *A* and *B*).

At 3 M KCl, the 18-repeat DHR10-mica18 assembles into a two-dimensional (2D) liquid-crystal–like phase similar to smectic or nematic phases with protein rods coaligned and ordered into discrete rows that persist for many hundreds of nanometers, whereas at only 100 mM KCl, protein rods form clustered domains along all three available axes in a phase not theoretically predicted for spherocylinders using hard-core models (25). This phase is not merely a kinetically trapped state, evidenced by its reversible transitions to and from this state upon adjusting ionic strength, suggesting that some specific protein–protein and/or protein–surface interaction must act to stabilize domains (23, 26). Furthermore, exchanging potassium for sodium increases the critical concentration at which the 2D liquid-crystal phase is formed, indicating a diminished binding affinity in sodium salt solution, and at low protein densities a dominant binding orientation is not obtained (Fig. 1*B*).

The principle of heteroepitaxial growth of proteins on muscovite appears to be quite general (21, 27, 28). For example, the engineered protein ^{C98}RhuA also shows surface-induced crystallization into condition-dependent morphologies (29) despite an apparent disagreement between the inherent C_4 symmetry of the protein and the *C*2/*c* symmetry of the pseudohexagonal muscovite surface. This occurs as the approximately square ($\sim 7 \times 7$ nm^2) proteins form corner-to-corner disulfide bonds to self-assemble into superstructures hundreds of nanometers across, locally oriented along either one or two directions depending upon solution concentrations of electrolytes as determined by AFM. Distinct crystalline morphologies can be selectively formed by tuning the concentrations and identity of the solution ions, despite using the same surface and building block (*SI Appendix*, Fig. S1) (29). The examples of DHR and RhuA systems clearly illustrate that protein–muscovite binding behavior can be extensively tuned via ion effects to control the pathways and outcomes of heteroepitaxial protein self-assembly. See

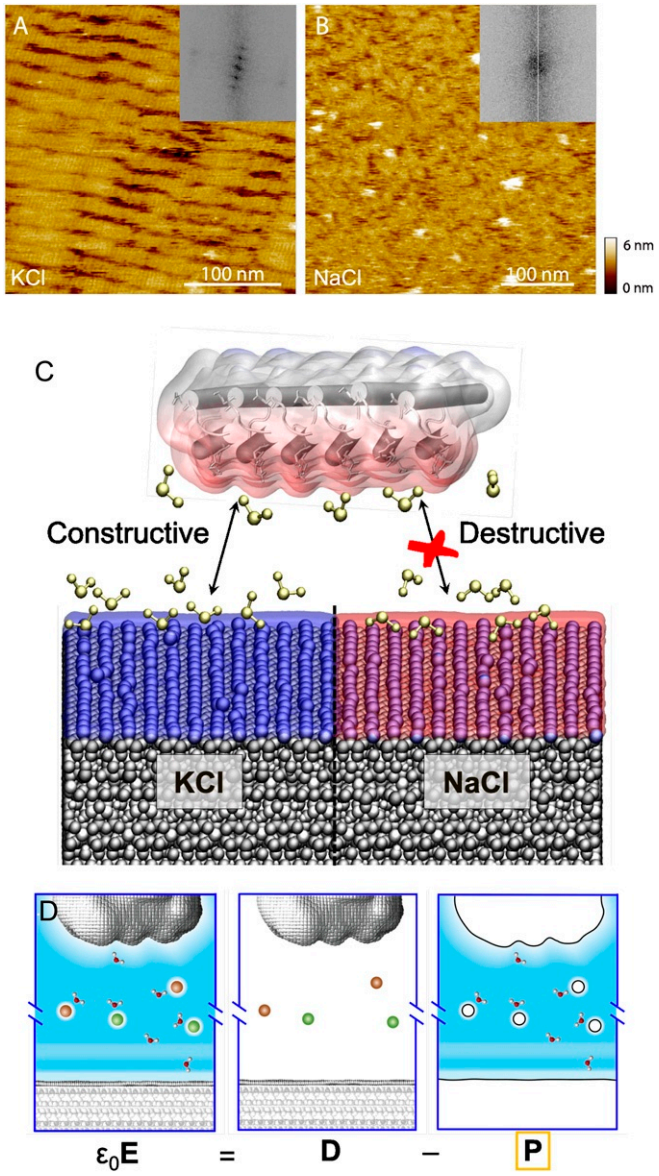

Fig. 1. (*A* and *B*) AFM images of DHR10-mica18 assembly. (*A*) The 0.1-μM DHR10-mica18 in 3 M KCl. (*B*) The 0.1-μM DHR10-mica18 in 3 M NaCl. *Insets* are fast Fourier transforms. The buffer is 20 mM Tris, pH 7. (*C*) Schematic representation of our key finding that macroscopic water polarization over muscovite is reversed in the presence of KCl vs. NaCl, which leads to either constructive or destructive interference with the polarization of a protein's surface, depending on specific ion effects. For DHR10-mica6 (shown) the relative attraction strengths of the protein's front or back faces to muscovite correlate with reduced orientational specificity observed in AFM (*B*). (*D*) Illustration of decomposing the total electric field **E** into displacement field **D**, consisting of background charges and the two surfaces (treated as fixed), and the electric polarization **P** due to water orientations, which is our focus here. This relation is written in SI units, where ε_0 is vacuum permittivity. Simulations of protein and muscovite are conducted separately.

SI Appendix, Fig. S2 for amino acid sequences and protein schematics.

The inability of theory to accurately predict a priori each outcome hinders the development of more sophisticated, hierarchically structured, assemblies. Simple hard-wall packing models fail to capture all of the necessary physics, as specific protein–surface and protein–protein interactions are not considered (25). Furthermore, high ionic strength conditions and specific ion effects are theoretically challenging even in the bulk

solution phase, as Debye–Hückel coefficients cannot account for electrolyte nonideality beyond dilute concentrations (30). The present work approaches this knowledge gap with the intent of first understanding the solvent-structuring properties of each assembly component in isolation to compute far-field surface–protein interactions (Fig. 1*C*).

We achieve this with three key modeling advancements:

1) We improve the accuracy of an empirical atomistic molecular dynamics (MD) model of muscovite mica relative to experiment by treating aluminosilicate substitutions using a pseudoatom with a mean-field philosophy, stoichiometrically averaging simulation parameters. Doing so enhances the chemical potential of muscovite for bound cations (a well-documented deficiency of empirical models at aqueous interfaces) (31, 32) and also eliminates measurement artifacts associated with specific substitution patterns.
2) We quantify aqueous response through the lens of local molecular-field (LMF) theory, which isolates the low-intensity, long-range component of electrostatic potential (33–36). Doing so resolves a dipolar solvent structure that is otherwise hidden beneath higher-intensity, short range contributions to the total signal. We apply this approach to measure far-field electric polarization (Fig. 1*D*).
3) We take the far-field polarization as measured from simulation as a scalar order parameter in the Landau free-energy expansion between two planar surfaces that induce forces on one another via solvent polarization (37, 38). Simulation data provide boundary values and a reference curve to fit an analytical solution of the order parameter and extract phenomenological parameters needed to compute the interaction pressure. By solving an analytical form of the Landau order parameter for asymmetric boundary conditions, we apply this approach to protein–surface interactions.

With this modeling approach, we quantify interaction strength between asymmetrically polarized surfaces via the long-range polarization-induced pressure and relate intrinsic far-field specific ion effects from atomistic simulations to experimentally observed changes in assembly outcome.

Accurate Mean-Field Model of Muscovite

In an effort to improve performance of the MD model relative to experiment, we compared the behavior of a standard atomistic representation of muscovite to its mean-field variant described here (both a 5 × 3 unit cell, using the INTERFACE force field [IFF]) (39). We analyzed molecular densities normal to the surface (z-axis density functions [ZDFs]) to determine the fraction of muscovite binding sites occupied by cations, which has been previously reported as underrepresenting the experimental limit of ∼100% (31, 40). At 3 M KCl the explicit-substitution model retains less than 85% of its first-layer cations, which are present on the surface in a bimodal distribution (Fig. 2*A*).

The mean-field model improves this occupancy to 97 ± 1% (Fig. 2*B*) and provides a hexagonal lateral pattern that matches AFM measurements (23), which is obscured in the explicit substitution variant because solvent patterning over muscovite is imprinted by the lateral positions of Al sites (Fig. 2 *C* and *D*). The mean-field treatment provides much more realistic depictions of the bulk-scale surface than standard explicit-substitution representations in terms of modeling the perfect hexagonal array of ions that proteins are designed against.

Further simulations were conducted on large (20 × 12 unit cell) slabs of IFF or CLAYFF (CFF) (41) mean-field muscovite, comparing solution conditions 3 M KCl to 3 M NaCl to mimic experiments. Measurements of molecular densities reveal subtle lateral inhomogeneity that persists despite the mean-field

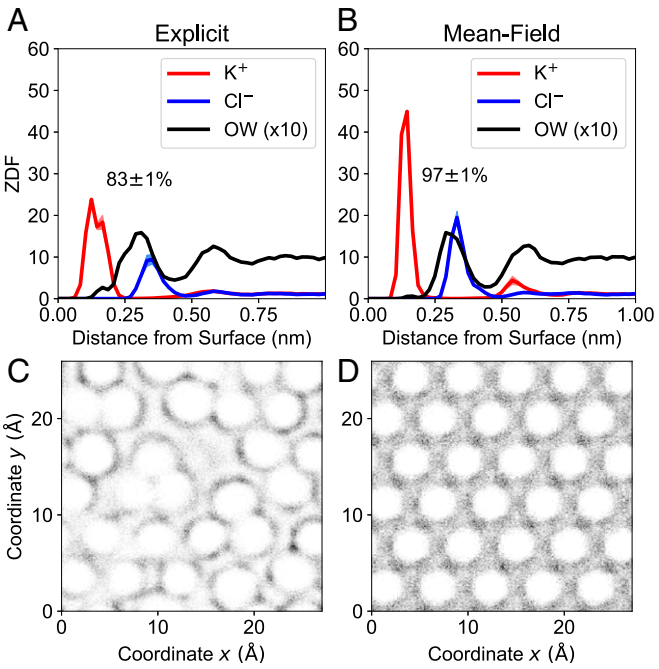

Fig. 2. For 3 M KCl aqueous conditions, we have (*A* and *B*) averaged probability density from atomic coordinates as a function of perpendicular distance from muscovite bedrock (ZDF), normalized to bulk, for (*A*) muscovite including explicit Al substitutions and (*B*) muscovite in the mean-field substitution representation. Both are using the INTERFACE force field. Percentages are fraction of cation binding sites occupied, measured by integrating up to the first minimum in the potassium density. (*C* and *D*) Average probability density of lateral water oxygen positions a distance of 3.0 ± 0.3 Å from the muscovite surface as measured from the surface-exposed oxygen atoms. Patterning is uneven under explicit Al substitution (*C*) and organized under the mean-field treatment (*D*).

treatment, which is reflective of the pseudohexagonal symmetry of muscovite (*SI Appendix*, Fig. S3). A lateral probability density of water oxygen within a narrow volume slice above the muscovite surface shows characteristic striping (Fig. 3). This finding is in alignment with prior simulation studies of parallel muscovite slabs at close separations, which show preference for a single alignment orientation that is mediated by multiple water layers (42). The anisotropy of muscovite has been experimentally shown to universally impose lateral asymmetry on the orientation of bound macromolecules, designed or natural (20, 21, 23, 29).

The attractions that give rise to surface assembly are complicated and numerous, but the electrostatic potential is particularly valuable here due to its slow decay. Solvent-structuring properties intrinsic to muscovite permeate far into the bulk and dominate the driving forces for macromolecules in solution, up to separations of ∼1 nm. Before short-range interactions (i.e., confinement effects) manifest, long-range assembly forces are responsible for orienting the preferred face pointed toward the surface. As a starting point for understanding assembly, we have focused on the dilute limit in which protein–protein interactions are negligible. This dilute limit coincides with experiments, which typically use less than 1 μM of protein [with mean interparticle separations $\mathcal{O}$(100 nm)], and indications of solution-phase protein–protein aggregation are absent. We also emphasize that polarization-induced interactions discussed here are long ranged and are the driving force until about 1 nm from the surface, at which point the protein cannot easily reorient. The many-body effect of multiple proteins interacting on the surface is beyond the scope of the current work.

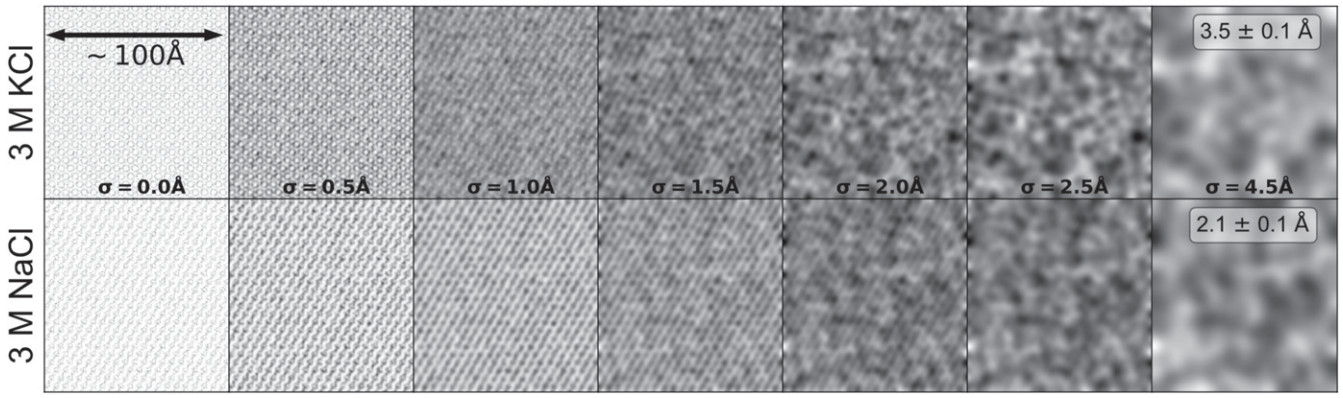

Fig. 3. Lateral probability distribution of water molecules occupying the narrow region of 3.5 ± 0.1 Å (*Top* row, 3 M KCl with IFF mean-field muscovite) or 2.1 ± 0.1 Å (*Bottom* row, 3 M NaCl with IFF mean-field muscovite). This same probability density is smoothed by a Gaussian of width σ (a KDE of probability), in columns *Left* to *Right*, from σ = 0.0 Å (no smoothing) to σ = 4.5 Å in increments of 0.5 Å. Characteristic streaking can be seen from the lower left to upper right corners of each panel, up to a smoothing length of about 2.0 σ. This illustrates that some distinctive atomistic signatures are inaccessible to far-field smoothing procedures that use Gaussians of width $\sigma = 4.5$ Å.

Quantifying Long-Range Solvent Response

We seek to isolate the far-field component of the full electrostatic potential computed from simulation, which is challenging to measure directly due to measurement noise over an intrinsically low-intensity interaction (43). By separating the slowly varying tail of the electric potential via the LMF formalism, we can accurately capture surface-induced electrostatic interactions that emanate far into the bulk (35). In practice, this is accomplished by taking a convolution of atomic point charges with a Gaussian kernel, as in the LMF smoothed charge density:

$$\rho^{\sigma}(\mathbf{r}) = \int \mathrm{d}\mathbf{r}'\rho(\mathbf{r}')\rho_G(\mathbf{r}-\mathbf{r}') \qquad [1]$$

$$\rho_G(\mathbf{r}) = \frac{1}{\pi^{3/2}\sigma^3}\exp\left(-|\mathbf{r}|^2/\sigma^2\right). \qquad [2]$$

The optimum value for the Gaussian width σ has been well studied and in aqueous solution is taken to be $\sigma = 0.45$ nm (34, 44). Because the density is being smoothed or filtered over a length scale, σ, that is larger than molecular scales, atomic-scale features of the muscovite surface are washed out in the far-field representation. To demonstrate, we take the lateral probability density of the water oxygens and filter it through a Gaussian kernel density estimate (KDE) of increasing width, σ, following Eq. **1**.

Lateral inhomogeneities observed in the oxygen density over muscovite persist when the signal is smoothed using a KDE Gaussian smoothing parameter from ∼0.5 up to about 2 Å, at which point the signal is laterally isotropic (Fig. 3). When using a Gaussian width of 4.5 Å for the LMF far-field analysis, lateral streaking is not observed, revealing that this striping tendency is a subtle near-field effect that cannot be captured using far-field dielectric theory. The same applies to explicitly substituted muscovite models, in which lateral inhomogeneities that arise from specific aluminosilicate substitution patterns are washed out by LMF smoothing (*SI Appendix*, Fig. S13).

Our present focus is in the direction of the surface normal, the vector along which a macromolecule approaches the surface. We use the macroscopic (or smoothed) polarization density as obtained through the LMF formalism as our order parameter. To access this quantity, we compute the atomistic electric polarization—the dipole moment per unit volume $\mathbf{P}(\mathbf{r}) = n(\mathbf{r})\langle\vec{\mu}(\mathbf{r})\rangle$ for an ensemble averaged water oxygen number density, $n(\mathbf{r})$, and an ensemble averaged water dipole vector as a function of spatial coordinates, $\langle\vec{\mu}(\mathbf{r})\rangle$ (45). By the divergence theorem, Gauss's law for the polarization density field can be written in differential form, which we apply twice to convert the polarization $P_{\hat{z}}(z)$ into the LMF smoothed bound charge density $\rho_b^{\sigma}(z)$ and then back to the LMF smoothed polarization (46):

$$\rho_b^{\sigma}(z) = -\frac{1}{4\pi}\int \mathrm{d}z'\partial_{\hat{z}}P_{\hat{z}}(z')\rho_G(z-z') \qquad [3]$$

$$P_{\hat{z}}^{\sigma}(z) = -4\pi\int \mathrm{d}z\ \rho_b^{\sigma}(z). \qquad [4]$$

The smoothed bound charge density $\rho_b^{\sigma}(z)$ is computed for these simulations over all space. For proteins, a rectangular region (visualized in *SI Appendix*, Fig. S4) was isolated as being confined between the protein's binding face and its periodic image along z. Signal from this rectangular subvolume was projected onto the z axis using an arithmetic mean in x/y to isolate signal arising from the protein.

In comparing intrinsic properties of muscovite under KCl vs. NaCl in the LMF representation, we find qualitative contrast between water polarization that is subtle to detect at the atomistic scale. Strikingly, the LMF signal (far-field electric polarization due to water) changes sign in the two cases, which can be seen in both $\rho_b^{\sigma}(z)$ and $P_{\hat{z}}(z)$ for muscovite (Fig. 4*A* and *B*). This finding has ramifications for all surface-induced organizational processes on muscovite, such as heterogeneous ice nucleation, which occurs more efficiently in KCl than in NaCl (47, 48). We seek to determine the impact of this unexpected field reversal on energetics of protein attraction.

In alignment with the Landau description of two surfaces at $z = \pm D/2$, we change the coordinate frame of reference such that opposing faces of a macromolecule are at either end of the unit cell, and bulk solution is at $z = 0$. A visual example is shown in Fig. 4*A*, where opposing surfaces at $z = \pm 30$ Å provide boundaries for the bulk. Simulations of proteins and muscovite individually were conducted in the same bulk environment, so charge density profiles can be concatenated together in bulk for a given salt treatment.

Theory for Polarization-Induced Interactions

Here we construct a theory for the polarization-induced forces felt by two planar surfaces with surface fields of arbitrary sign and intensity. For this we use a Landau theory framework described in detail by Netz and coworkers (37, 38, 49). The theory is built on a free-energy density expansion about a general order parameter η that describes the response of the solvent to two planar surfaces that are fixed at $z = \pm D/2$. Within Landau theory, the surface

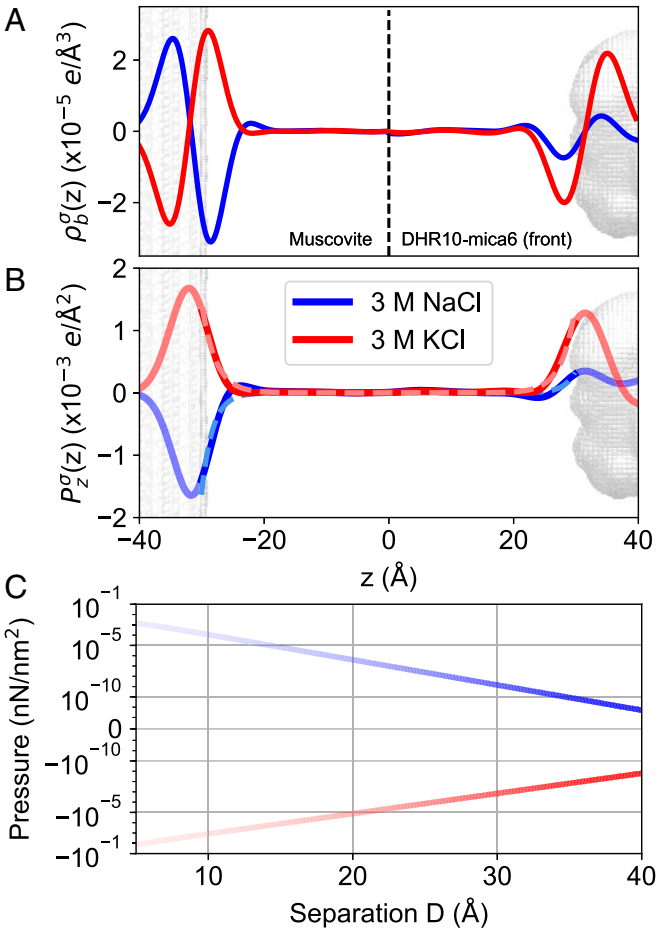

Fig. 4. Demonstration of converting $\rho_b^\sigma(z)$ obtained from LMF-processed MD trajectories into polarization-induced pressure between muscovite and the front/back faces of DHR10-mica6. (*A*) A concatenated bound charge density profile is made by adjoining partial $\rho_b^\sigma(z)$ profiles from trajectories of protein or muscovite in isolation at the bulk, where solution conditions are identical. (*B*) We compute $P_z^\sigma(z)$ from $\rho_b^\sigma(z)$ via Eqs. **3** and **4** as in the main text and then fit the functional form of order parameter $\eta(z)$ (Eq. **6**) to polarization on the region [−30 Å, +30 Å] that is solvent accessible (fits are dashed lines). (*C*) Fitting $\eta(z)$ to $P_z^\sigma(z)$ determines the phenomenological parameters needed to evaluate pressure Π (Eq. **9**) as a function of separation *D*, where a positive Π indicates repulsion. In *A–C*, red coloration indicates 3 M KCl solution, while blue indicates 3 M NaCl.

groups give rise to a surface field, $h_\pm$ for the surface at $z = \pm D/2$. To be consistent with the literature, we derive the Landau theory for a general order parameter $\eta(z)$, with the understanding that this refers to the far-field polarization for the problem of interest. In this case, we can write down the Landau free energy (per unit area) as

$$\frac{\mathcal{F}}{A} = \int_{-D/2}^{D/2} \mathrm{d}z \left[a\eta^2(z) + c(\eta'(z))^2\right] + h_+\eta(D/2) + h_-\eta(-D/2), \quad [5]$$

where $\eta'(z)$ is the derivative of $\eta(z)$ with respect to z, and a and c are phenomenological parameters that give measure of the stiffness of the order parameter and the spatial range of interactions, respectively. The parameter a is a property of the bulk solvent, and when polarization is in the relevant order parameter, one can show that $a = (1 - 1/\varepsilon)/2\varepsilon_0$, where ε is the static dielectric constant of the solvent and ε_0 is the vacuum permittivity, as shown in *SI Appendix*.

The functional form of $\eta(z)$ is determined by minimizing the free-energy density with respect to the order parameter, giving a family of solutions for different boundary conditions (BCs). Prior work has used symmetric ($h_+ = h_- = h$) or antisymmetric ($h_+ = -h_- = h$) BCs. Here we solve for a more general solution of $\eta(z)$, making no assumptions about the signs or relative magnitudes of $h_\pm$, and use this solution to determine the polarization-induced pressure Π. We work at fixed surface field $h_\pm$ and define $\eta(D/2) = \eta_R$ and $\eta(-D/2) = \eta_L$ at the boundaries. We obtain the following expression for the order parameter profiles,

$$\eta(z) = \eta_R \frac{\sinh\left(\frac{D}{2\lambda} + \frac{z}{\lambda}\right)}{\sinh(D/\lambda)} + \eta_L \frac{\sinh\left(\frac{D}{2\lambda} - \frac{z}{\lambda}\right)}{\sinh(D/\lambda)}, \quad [6]$$

where $\lambda = (c/a)^{1/2}$. With $\eta(z)$ at the free-energy minimum known, we are able to determine the surface fields h_+ and h_-,

$$h_\pm = -\frac{2c}{\lambda}[\eta_{R/L}\coth(D/\lambda) - \eta_{L/R}\mathrm{csch}(D/\lambda)]. \quad [7]$$

Substituting Eqs. **6** and **7** into Eq. **5** allows $\mathcal{F}/A$ to be evaluated in terms of surface fields $h_\pm$ and physical constants a and c for some separation D:

$$\frac{\mathcal{F}}{A} = \frac{-(h_+h_-)}{2(ac)^{1/2}}\coth\left(\frac{D}{2\lambda}\right)\left[1 + \frac{(h_+ - h_-)^2}{2h_+h_-}\frac{\coth(D/\lambda)}{\coth(D/2\lambda)}\right]. \quad [8]$$

We can now evaluate the polarization-induced pressure between the surfaces as

$$\Pi(D) = -\frac{d(\mathcal{F}/A)}{dD} = -\frac{h_+h_-}{4c}\mathrm{csch}^2\left(\frac{D}{2\lambda}\right)\left[1 + \frac{(h_+ - h_-)^2}{h+h_-}\frac{\sinh^2(D/2\lambda)}{\sinh^2(D/\lambda)}\right]. \quad [9]$$

In this notation a negative pressure is attractive and occurs when h_+ and h_- are of the same sign. For large D, the pressure scales as

$$\Pi \sim -\frac{h_+h_-}{c}e^{-D/\lambda}\left[1 + \frac{(h_+ - h_-)^2}{h_+h_-}e^{-D/\lambda}\right], \quad [10]$$

which indicates an exponentially decaying attraction at the largest D values.

When the surfaces are asymmetric, $|h_+| \neq |h_-|$, a second relevant length scale of $2D/\lambda$ emerges that can compete with the behavior of the pressure on a scale of D/λ, and this results in a nontrivial change in the sign of Π at

$$D/\lambda = 2\cosh^{-1}\left(\sqrt{\frac{-(h_+ - h_-)^2}{4h_+h_-}}\right) \sim \ln\left(\frac{-(h_+ - h_-)^2}{h_+h_-}\right). \quad [11]$$

The functional form of this intercept bounds the relative values of $h_\pm$ for a crossing to occur on $D > 0$. For example, Eq. **11** is undefined for either symmetric or antisymmetric $h_\pm$, and so this was absent in previous work. An intercept is present for all $h_+h_- < 0$ if $h_+ \neq -h_-$ and occurs at greater D/λ for ratios of $h_\pm$ far from unity. In the present work, where λ is on the order of 2 Å, each instance that matched these criteria produced intercepts at $D/\lambda < 5$ Å and so may not be relevant to the far-field descriptors provided here. A detailed derivation of this theory and further discussion is provided in *SI Appendix*.

There are two major results from this derivation: 1) By solving an analytical $\eta(z)$ (Eq. **6**) for asymmetric BCs we can fit the

functional form of $\eta(z)$ to $P_{\hat{z}}(z)$ computed from simulation, and 2) the parameters determined from fitting to data (surface fields and λ) can be inserted into $\Pi(D)$ (Eq. **9**), which provides an estimate of distance-dependent behavior.

It is apparent that, on the domain of z that is solvent accessible, the function $P_z^\sigma(z)$ has a sinh-like form that can be well approximated by the analytical function $\eta(z)$. The fitted function $\eta(z)$ is overlaid in Fig. 4*B* to illustrate. We take the parameters η_R and η_L from $P_z^\sigma(\pm D/2)$ and fit λ, which here ranges from 1.66 to 2.21 Å, larger than similar results for membranes (38). The extracted parameter λ permits the pressure $\Pi(D)$ to be estimated for a given polarization profile.

For discrete simulations of mean-field muscovite or protein isolated in 3 M aqueous KCl or NaCl, we computed $P_z^\sigma(z)$ for each surface. At large z these polarization densities are the same (for a given ion treatment) and so a composite $P_z^\sigma(z)$ is generated by concatenating intrinsic polarization in the bulk region. The composite systems consist of the muscovite surface parallel to a flat protein face, either the notional binding face or the reverse side. Comparing results under KCl and NaCl conditions reveals qualitatively different far-field muscovite–protein interactions.

Fig. 5 shows selected $\Pi(D)$ profiles for composite muscovite–protein systems. The notional binding face of ^{C98}RhuA is attracted to muscovite under both KCl and NaCl conditions, as indicated by the negative $\Pi(D)$. In contrast, the notional binding face of DHR10-mica6 is strongly attracted to muscovite under KCl conditions but is repelled in NaCl solution. The reverse is true of the backside of DHR10-mica6, which is not attracted to muscovite in the presence of KCl but is with NaCl. The qualities of these pressure profiles are determined by the relative

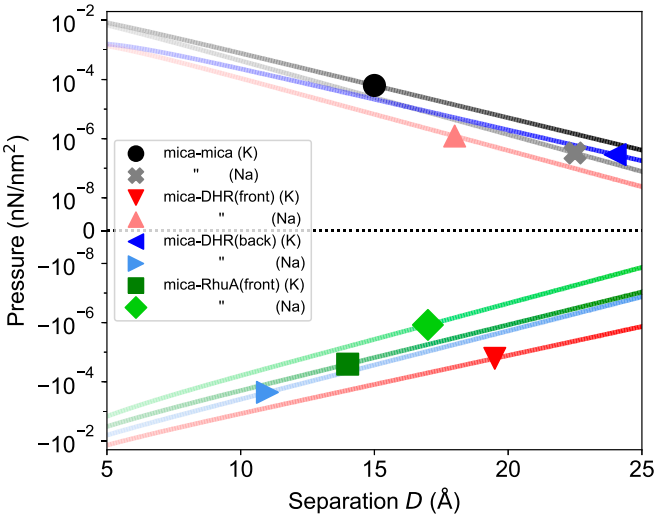

Fig. 5. Selected far-field polarization-induced pressure curves demonstrating impacts of K^+/Na^+ exchange. The eight traces presented are to be thought of as four pairs, each representing a given muscovite–macromolecule pair under both 3 M KCl and 3 M NaCl conditions. These macromolecule pairings are muscovite–muscovite (as reference, in black), muscovite–DHR$_{binding}$ (red), muscovite–DHR$_{back}$ (blue), and muscovite–^{C98}RhuA$_{binding}$ (green). Pairs of traces are indicated by a shared color (dark vs. light shade for KCl vs. NaCl, respectively) and corresponding symbols, (●, ✖), (▼, ▲), (◄, ►), (■, ♦), listed in KCl/NaCl order. For example, the red pair of traces (▼, ▲) corresponds to those in Fig. 4*C*. With $\Pi > 0$ indicating repulsion we see muscovite–muscovite is repulsive under both KCl and NaCl, muscovite–^{C98}RhuA$_{binding}$ is attractive in both cases, and the muscovite–DHR interaction can be modulated to attractive or repulsive depending on which protein face is presented and the salt treatment. See *SI Appendix*, Fig. S2 for renderings of the two proteins to illustrate the notional front and back faces.

signs and magnitudes of the surface fields generated by each body intrinsically, which can be explained with atomistic evidence from simulation. These results are consistent with experimental findings as detailed in *Discussion*.

Consistency with Atomistic Interpretations

One of the principal findings reported here is the change in sign of the far-field components of electric polarization due to water when K^+ is exchanged for Na^+ over muscovite. Considering that both systems consist of an ionic double layer with cations bound to mica, it is perhaps surprising that such a polarization reversal should occur. This observation can be reconciled with atomistic data: There are more surface vacancies for water molecules under NaCl conditions (as seen in *SI Appendix*, Fig. S5, close to the surface). Water molecules occupying cation binding pockets have a strong tendency to orient with the positive end of the dipole toward mica (*SI Appendix*, Fig. S6). Conversely, water molecules slightly farther from the surface tend to interact strongly with the bound cations and so orient their negative end toward the mica. By virtue of having more ion binding vacancies, the Na^+ condition sees a shift in relative intensity between these two populations of water molecules.

Furthermore, the presence of a secondary density peak in atomistic Na^+ position data reveals that the ionic double layer is less well organized than with K^+ and fails to attract counterions as intensely (*SI Appendix*, Fig. S5). This gives rise to a broad orientational distribution of water at the interface, particularly ∼0.5 nm from the surface, and peaks in the water oxygen density function correspond to local water orientations opposite that of K^+ (*SI Appendix*, Fig. S6). This is all to say that the LMF far-field polarity reversal on muscovite is consistent with the underlying atomistic structural changes.

The other intrinsic property of muscovite reported here, lateral anisotropy, does not contribute to far-field interactions as evidenced in Fig. 3. The heights above muscovite at which lateral anisotropy can be detected are narrow, indicating that these streaking effects may be felt by macromolecules only when adsorbed. The finding of this lateral anisotropy does not contradict a previous AFM study of the azimuthal dependence interaction between two disjoining mica surfaces (50). In ref. 50 the force between the two mica surfaces was measured at a predicted separation of roughly 1 nm. At this separation a weak azimuthal dependence of the force between the mica surfaces is observed, reflecting the underlying basal symmetry of mica. However, no lateral anisotropy was recorded that is consistent with Fig. 3. The predicted separation of 1 nm between the two surfaces in ref. 50 is likely too great a distance to sense the short-range lateral anisotropy. Moreover, it was suggested that the weak azimuthal dependence of the force between mica surfaces at separations of ∼1 nm cannot be predicted with electrostatics alone (42, 50). To the extent that the protein–mica surfaces remain close enough to sense the lateral anisotropy in Fig. 3 is possible due to the polarization-induced forces predicted in Fig. 5. This is distinct from ref. 50 where two mica surfaces were found to feel a repulsive long-range interaction (*SI Appendix*, Fig. S10) and therefore remain farther apart. Additional study is needed to assess the interplay of lateral streaking and polarization along the normal, which here are presented as distinct observations. The ramifications of these striking features are currently being analyzed through the lens of close-range protein/surface interactions in a separate body of work.

Differences in LMF signal near the faces of proteins can be corroborated atomistically as well. For example, when K^+ is exchanged for Na^+, the binding face of DHR10-mica6 experiences an approximately two- to threefold deamplification in water polarization density $P_z^\sigma(z)$ (Fig. 4*A*). This signal aligns with atomistic density distributions, which reveal a competition

between cations and water molecules at the protein surface. While sodium ions show a marginally stronger affinity for the protein binding face than potassium, this is balanced with a depletion in the water density profile and waters farther from the surface showing a diminished angular preference. Density profiles on either side of DHR10-mica6 are included in *SI Appendix*, Fig. S7 and the consequent water orientation distributions are shown in *SI Appendix*, Fig. S8. Thus, atomistic simulations of a lone macromolecule in solution can provide sufficient information to predict surface adsorption behavior by evaluating the compatibility of its far-field response (due to atomic-scale structuring near the molecule) with those arising from the solid–liquid interface. Such relationships are challenging to disentangle without LMF analysis.

Discussion

Analyzing MD data through the lens of LMF theory has allowed us to connect intrinsic polarization to assembly processes via induced pressure from Landau theory. The unexpected activity of the DHR10-mica6 "back face" in NaCl results in an attractive $\Pi(D)$ as the protein approaches the surface with this orientation, in contrast to the binding face that interacts very weakly with muscovite in NaCl (Fig. 5). The low-intensity nature of far-field interactions means that these directional electrostatic biases on the protein are perturbations to its orientational distribution with respect to muscovite. These predictions are valid at large D, as eventually short-range interactions become nonnegligible and intrinsic far-field properties might interfere nonlinearly. These bound-state interactions will be characterized explicitly in a separate study.

The observation that the DHR10-micaX back face becomes well ordered in NaCl conditions leads to the hypothesis that DHR10-micaX proteins may have substantive populations bound to muscovite through both of the protein faces in NaCl. This contrasts with KCl conditions in which the binding face designed to match the muscovite potassium ion sublattice is expected to dominate. The back face of DHR10-micaX is not designed to match the muscovite lattice, which reduces the tendency for the protein to align along any of its pseudohexagonal axes. Indeed, experimental observations suggest diminished orientational specificity of protein binding in NaCl solution on average. AFM results show that the protein DHR10-mica18 displays weaker orientational specificity in aqueous NaCl than in KCl (Fig. 1). Furthermore, the most intense protein–muscovite interaction as predicted by $\Pi(D)$ is with the binding face of DHR10-micaX under KCl conditions, and our predictions are consistent with the experimentally observed increase in critical concentration required to reach a 2D liquid crystal in NaCl solutions.

The other muscovite-binding protein ^{C98}RhuA has a relatively flat binding face and contacts muscovite under both KCl and NaCl conditions, as demonstrated by AFM experiments (29, 51, 52). Our theory predicts that ^{C98}RhuA displays a weak attraction to muscovite from afar via $\Pi(D)$ in both cases (Fig. 5). The lack of spatial ordering on the face of ^{C98}RhuA compared to muscovite, combined with the highly screened environment studied here, results in weak polarization, $P_z^\sigma(z)$. This polarization in response to ^{C98}RhuA is dependent on the size of the subvolume used for analysis (*SI Appendix*, Fig. S9), unlike DHR10-mica6. This is due to patterning of amino acids on and the curvature of the binding face of ^{C98}RhuA. These two effects wash out the signal from highly charged residues at the center and our predictions for ^{C98}RhuA can be improved through three-dimensional order parameters. The large asymmetry between surface fields at muscovite and ^{C98}RhuA surfaces results in pressure profiles with a nontrivial zero crossing at finite D that may be relevant for assembly. This nonmonotonic form of $\Pi(D)$ occurs only for asymmetric surfaces; see *SI Appendix* for further discussion on competing length scales that emerge when the polarization profile is asymmetric.

The magnitudes of the polarization-induced pressures and characteristic length scales reported here are similar to those reported in other computational, theoretical, and experimental studies (42, 50, 53–56). Measurements of pressure between two separated muscovite slabs vary, depending on methodology and conditions, with estimates that are higher or lower than what is reported here at ∼2 nm separation. In particular, the result depends sensitively on the double layer's screening of the surface, which seems to be underestimated in empirical simulation models, compared to experiment. Our predictions are consistent with pressure estimates available in the literature, and a discussion on comparisons among pressure estimates is given in *SI Appendix*, section 4.

Conclusion

In this work we have shown how the intrinsic solvent-structuring properties of minerals and proteins with flat surfaces can be connected via a theoretical framework to categorize far-field interactions as attractive or repulsive for a given protein orientation. Relative interaction strengths in this picture correlate well with experimental observations of surface assembly. We construct an empirical all-atom muscovite model with improved cation occupancy (as a percentage of available sites) to compute solvent polarization in response to specific ion effects. The combined simulation/theoretic framework presented is broadly applicable to surface assembly problems and to predict a macromolecule's orientation upon approach.

The philosophy of this work takes water molecules as reporters for the underlying electric fields generated by ion organization in the vicinity of a liquid–solid interface. That is, by studying electric polarization rather than the entire electric field, we avoid boundary condition issues that arise from Poisson–Boltzmann analyses and omit the electric displacement field associated with ρ_{unbound}. The Landau theory approach taken here is advantageous because inputs are computed directly from simulation. While the present work demonstrates the efficacy of this strategy in high-concentration alkali salts in order to emulate experiments, we emphasize that this computational strategy is generally applicable to surfaces without well-ordered ion double layers at more typical ionic strengths.

One of the key findings from these simulations is that exchanging the identity of the aqueous salt from KCl to NaCl over muscovite results in a sign reversal in far-field electrostatic measurements ρ_b^σ and P_z^σ due to water molecules. This sign reversal can be understood as arising from the multibinding-well character of Na^+ on muscovite, an observation that has been corroborated in x-ray reflectivity measurements (57). Such a sign reversal is likely not exclusive to muscovite and may occur on related clay surfaces (i.e., montmorillonite, kaolinite, etc.) due to differences in surface organization for each ion.

This finding leads us to consider other polarization changes that occur on mineral-binding proteins that would impact the ability of the binding face to specifically orient toward the surface when approaching from solution. Qualitative changes to the long-range component of the electrostatic potential due to water are observed at some protein faces but not others, highlighting the importance of computing intrinsic properties from atomistic simulations. Furthermore, while atomistic measurements corroborate the LMF picture, this processing is essential to disambiguate the far-field character.

Ion-specific differences in surface polarization are potentially exploitable properties in engineering self-assembling materials: Taken in conjunction with high-intensity close-range interactions that do not flip sign with exchanging salt, it may be plausible

to dynamically control heteroepitaxial growth by modulating salt conditions to amplify or deter far-field attraction while not disrupting the bound layer.

While the present work focuses on protein–surface interactions on nanometer length scales by extracting the far-field, macroscopic polarization, it is in principle possible to extend this framework to capture short-range oscillatory behavior in Landau theory as well. This combined simulation-theoretic approach will be valuable in coming to a predictive understanding of the conditions in which proteins assemble on surfaces. The simulations required to extract intrinsic surface properties are simple to conduct and inexpensive, providing a potential high-throughput route to assessing the driving forces of assembly.

Materials and Methods

The geochemistry of muscovite is well studied for the bulk material and reliable all-atom MD force fields have been published, particularly IFF (39) and CFF (41). However, there are a number of practical issues with capturing the structural characteristics of the liquid–muscovite interface using either model: 1) The chemical potential of ion adsorption does not agree with experimental observation at low concentration and surface ion occupancy is underrepresented; 2) ion adsorption at the interfacial double layer depletes the aqueous environment due to finite size effects; and 3) lateral organization of water and ions is sensitive to aluminum substitution patterns within muscovite, which may be assigned in a variety of ways. These are addressed as follows:

1) The fraction of surface cation binding sites that are occupied vs. vacant is underrepresented in MD simulation compared to experiment (both CFF and IFF), which is combated by utilizing a high chemical potential aqueous bath: Here we use 3 M monovalent salt, emulating experimental conditions in which DHR10-mica6 and ^{C98}RhuA bind muscovite. The high salinity simulated here is in emulation of experimental surface coverage near 100% occupancy, an overcharged surface with a strong ion double layer (23). High occupancy is maintained down to 1 M salt, at which point competition from hydronium ions becomes an important factor, a situation that cannot be accurately captured in classical simulation.
2) Freshly cleaved, electrically neutral muscovite (as is prepared in default IFF or CFF repositories) includes only 50% of available cation sites occupied. When exposed to solution, vacancies are populated with ions from the bath. To prevent the finitely sized aqueous bath in MD from being depleted of ions due to surface sequestration, while also avoiding an enormous simulation box, the aqueous phase is prepared in MD with the anticipation that some number of ions will adsorb to the surface. That is, a simulation of aqueous muscovite includes sufficiently many ions to both 100% saturate the muscovite surface and maintain the desired aqueous concentration.
3) The lateral positioning of surface-exposed Al substitution sites (prevalent at a 1:3 stoichiometric ratio with Si) is adjustable and measured lateral inhomogeneities correlate with the substitution pattern chosen. To prevent measurement artifacts associated with specific Al distributions and to match ion distributions that mica-binding proteins are designed against, a mean-field approach is presented. Where explicit substitutions are used for comparison, the NMR-derived random pattern from IFF is preferred.

In this work we combine Si and Al into a statistically representative pseudoatom, which removes lateral Al organization from consideration when conceptualizing far-field interactions. Briefly, this mean-field pseudoatom approach was accomplished by taking 1:3 weighted averages of the parameters for Al and Si. Conveniently, some parameters such as the Lennard-Jones well depth ϵ are identical for Al and Si both in CFF and IFF, and so the statistical average is trivial. In both CFF and IFF the radius σ was taken to be a weighted arithmetic mean of Al and Si, following the Lorentz–Berthelot combination rule (58). Mass and charge were averaged similarly, for example yielding mass: $(3 \times m_{Si} + 1 \times m_{Al})/4 = 27.25764$ amu. The CFF topology does not include explicit bonds linking inorganic bodies, and so for CFF no further adjustments are required. Within IFF, such bond and angle definitions do exist, but parameters are identical for Si or Al in the same environment. Finally, oxygen atoms adjacent to substitution sites have their partial charges adjusted as well, in the same mean-field philosophy of lateral homogeneity.

Slabs of mica were prepared three double layers thick ($\approx$6 nm total) to thoroughly insulate periodic images from one another. To further ensure that the muscovite slab did not bend due to thermal fluctuations, 1,000 kJ/mol harmonic restraints were placed on a single layer of potassium ions embedded nearest the surface's center. This way, the surface as a whole retains its planar geometry while leaving surface layers flexible to respond to solvent. Models were constructed from the force field to a 5×3 unit cell lattice ($\sim 2.6 \times 2.7$ nm^2) or a 20×12 unit cell lattice ($\sim 10.4 \times 10.8$ nm^2). The larger simulation cell is beneficial for identifying lateral inhomogeneities that persist despite usage of the mean-field Al substitution treatment, which would be reflective of the asymmetric hexagonal surface structure of muscovite.

Solvent-exposed alkali metal parameters were taken from the work of Joung and Cheatham (JC) (59), which have been specifically parameterized to prevent crystallization at high concentration (up to 3 M in this work). Protein simulations were conducted with the well-established Chemistry at Harvard Macromolecular Mechanics (CHARMM) 36 force field (60). The CHARMM family of force fields was developed for use with the CHARMM-modified transferable intermolecular potential with 3-points (TIP3P) water model (mTIP3P), which differs from the original TIP3P by the addition of Lennard-Jones sites to the hydrogen atoms. To apply the mTIP3P water model to CHARMM-based proteins while retaining the original TIP3P behavior with JC ions, nonbonded fix (NBFIX) was used to set Lennard-Jones interactions to zero only for water hydrogen–ion pairs (61). Doing so permits JC ions to interact with original TIP3P water while permitting the protein to interact with mTIP3P.

Proteins were restrained at four alpha carbons using harmonic potentials within Groningen Machine for Chemical Simulations (GROMACS) (1,000 kJ/mol spring constants) to keep a fixed frame of reference. The restrained sites were selected to be at opposite corners of the protein to prevent tumbling motions, while permitting side-chain and protein loop fluctuations to thoroughly sample interactions with the aqueous environment. For DHR10-mica6 these were alpha carbons 8A, 150A, 180A, and 258A, while for ^{C98}RhuA these were 79F on each tetrameric subunit.

Simulations were conducted using GROMACS 2018.3 (62, 63). All simulations described utilized particle mesh Ewald electrostatics with 0.08 nm Fourier spacing, with neighbor list and electrostatics cutoffs at 1.0 nm, and were conducted at 300 K. The Berendsen barostat was employed for isothermal–isobaric (NPT) ensemble equilibration over 25 ns with bulk compressibility 0.000045 normal to the surface (z) and semiisotropic coupling preventing deviations in x/y. The full equilibration period is required to ensure that ions initialized in the bulk phase have sufficient time to adsorb onto the surface prior to 100 ns of production canonical (NVT) ensemble. For the proteins, only 15 ns NPT equilibration is required since these proteins do not sequester ions the same way muscovite does. However, a total of 150 ns of NVT simulation were conducted due the lower symmetry (and therefore reduced data quality) of proteins compared to muscovite. Error bars were computed by the method of bootstrapping, subdividing the simulated trajectory into 10 nonoverlapping subsections and computing standard deviations from the repeated results.

For slabs of muscovite only 5×3 wide, the system was sufficiently small to perform Parallel-Bias Well-Tempered Metadynamics with Partitioned Families (PBMetaD-PF) (64). Briefly, this technique includes a time-dependent energetic bias on the z coordinates of all K^+ and Cl^- ions using the redundancy of their coordinates to converge the bias potential in little time. Biasing ion z coordinates in this way expedites the exploration of phase space and can reveal hidden energetic basins. PBMetaD-PF used Gaussian width sigma 0.01, with bias factor 5, initial hill height 1.25 kJ/mol, and pace 500 steps, at a target temperature of 300 K in accordance with previous ion-binding potential of mean force (PMF) studies (65). Production runs were on the time scale of 200 ns in the NVT ensemble. Due to the fact that $\sim$150 ions of each kind contribute to each PMF, many may be surface bound at once, and typical cation residence times are on the order of nanoseconds, convergence was quickly achieved (*SI Appendix*, Fig. S10). We concluded that further PBMetaD-PF would not be required.

Data Availability. All study data are included in this article and/or *SI Appendix*.

ACKNOWLEDGMENTS. The AFM experiments were done in Pacific Northwest National Laboratory (PNNL). PNNL is a multiprogram national laboratory operated for the Department of Energy by Battelle under Contract DE-AC05-76RL01830. We thank Sebastien Kerisit for providing simulation data for comparative purposes. We acknowledge helpful conversations with Greg Schenter, Jaehun Chun, Lilo Pozzo, Andy Ferguson, Xin Qi, Mingfei Zhao, Sarah Alamdari, Janani Sampath, and Orion Dollar. This work was

facilitated through the use of advanced computational, storage, and networking infrastructure provided by the Hyak supercomputer system at the University of Washington. This material is based on work supported by the US Department of Energy, Office of Science, Office of Basic Energy Sciences, as part of the Energy Frontier Research Center program, the Center for the Science of Synthesis Across Scales under Award DE-SC0019288.

1. M. Frank, D. Drikakis, Thermodynamics at solid-liquid interfaces. *Entropy* **20**, 362 (2018).
2. C. Sievers *et al.*, Phenomena affecting catalytic reactions at solid-liquid interfaces. *ACS Catal.* **6**, 8286–8307 (2016).
3. R. M. Hazen, D. A. Sverjensky, Mineral surfaces, geochemical complexities, and the origins of life. *Cold Spring Harb. Perspect. Biol.* **2**, a002162 (2010).
4. G. W. Achtersh Auser, Before enzymes and templates: Theory of surface metabolism. *Microbiol. Rev.* **52**, 452 (1988).
5. F. Nudelman, N. A. Sommerdijk, Biomineralization as an inspiration for materials chemistry. *Angew. Chem. Int. Ed.* **51**, 6582–6596 (2012).
6. Y. Chen *et al.*, Biomineralization forming process and bio-inspired nanomaterials for biomedical application: A review. *Minerals* **9**, 68 (2019).
7. J. Jiang, K. Hirano, K. Sakurai, Interface-sensitive imaging by an image reconstruction aided x-ray reflectivity technique. *J. Appl. Crystallogr.* **50**, 712–721 (2017).
8. L. Dalstein, K. Y. Chiang, Y. C. Wen, Direct quantification of water surface charge by phase-sensitive second harmonic spectroscopy. *J. Phys. Chem. Lett.* **10**, 5200–5205 (2019).
9. T. Fukuma, R. Garcia, Atomic-and molecular-resolution mapping of solid-liquid interfaces by 3d atomic force microscopy. *ACS Nano* **12**, 11785–11797 (2018).
10. X. Zhang *et al.*, Direction-specific interaction forces underlying zinc oxide crystal growth by oriented attachment. *Nat. Commun.* **8**, 835 (2017).
11. M. Ricci, W. Trewby, C. Cafolla, K. Voitchovsky, Direct observation of the dynamics of single metal ions at the interface with solids in aqueous solutions. *Sci. Rep.* **7**, 43234 (2017).
12. A. M. Smith, A. A. Lee, S. Perkin, The electrostatic screening length in concentrated electrolytes increases with concentration. *J. Phys. Chem. Lett.* **7**, 2157–2163 (2016).
13. L. Liu *et al.*, Connecting energetics to dynamics in particle growth by oriented attachment using real-time observations. *Nat. Commun.* **11**, 1045 (2020).
14. M. Goedert, Alzheimer's and Parkinson's diseases: The prion concept in relation to assembled ab, tau, and α-synuclein. *Science* **349**, 6248 (2015).
15. D. Li *et al.*, Direction-specific interactions control crystal growth by oriented attachment. *Science* **336**, 6084 (2012).
16. J. J. McManus, P. Charbonneau, E. Zaccarelli, N. Asherie, The physics of protein self-assembly. *Curr. Opin. Colloid Interface Sci.* **242**, 73–79 (2016).
17. E. N. Salgado, R. J. Radford, F. A. Tezcan, Metal-directed protein self-assembly. *Acc. Chem. Res.* **43**, 661–672 (2010).
18. Q. Luo, C. Hou, Y. Bai, R. Wang, J. Liu, Protein assembly: Versatile approaches to construct highly ordered nanostructures. *Chem. Rev.* **116**, 13571–13632 (2016).
19. K. Curry, Mica. *US Dep. Interior Geol. Surv.* **24**, 49.1–49.10 (2017).
20. S. Woo, P. W. K. Rothemund, Self-assembly of two-dimensional DNA origami lattices using cation-controlled surface diffusion. *Nat. Commun.* **5**, 4889 (2014).
21. W. W. Leow, W. Hwang, Epitaxially guided assembly of collagen layers on mica surfaces. *Langmuir* **27**, 10907–10913 (2011).
22. T. Brunette *et al.*, Exploring the repeat protein universe through computational protein design. *Nature* **528**, 580–584 (2015).
23. H. Pyles, S. Zhang, J. J. D. Yoreo, D. Baker, Controlling protein assembly on inorganic crystals through designed protein interfaces. *Nature* **571**, 251–256 (2019).
24. S. Zhang *et al.*, Engineering biomolecular self-assembly at solid–liquid interfaces. *Adv. Mater.* **33**, 1905784 (2020).
25. M. A. Boles, M. Engel, D. V. Talapin, Self-assembly of colloidal nanocrystals: From intricate structures to functional materials. *Chem. Rev.* **116**, 11220–11289 (2016).
26. S. Whitelam *et al.*, Common physical framework explains phase behavior and dynamics of atomic, molecular, and polymeric network formers. *Phys. Rev. X* **4**, 011044 (2014).
27. D. M. Czajkowsky, L. Li, J. Sun, J. Hu, Z. Shao, Heteroepitaxial streptavidin nanocrystals reveal critical role of proton "fingers" and subsurface atoms in determining adsorbed protein orientation. *ACS Nano* **6**, 190–198 (2012).
28. R. W. Loo, M. C. Goh, Potassium ion mediated collagen microfibril assembly on mica. *Langmuir* **24**, 13276–13278 (2008).
29. S. Zhang, R. Alberstein, J. D. Yoreo, F. A. Tezcan, Assembly of a patchy protein into variable 2d lattices via tunable, multiscale interactions. *Nat. Commun.* **11**, 3770 (2020).
30. M. R. Wright, "Debye-Huckel and Fuoss-Onsager equations" in *An Introduction to Aqueous Electrolyte Solutions*, A. Slade, R. Ballard, R. Hambrook, Eds. (John Wiley & Sons, West Sussex, United Kingdom, 2007), pp. 1–29.
31. D. Martin-Jimenez, E. Chacon, P. Tarazona, R. Garcia, Atomically resolved three-dimensional structures of electrolyte aqueous solutions near a solid surface. *Nat. Commun.* **7**, 1–7 (2016).
32. D. Martin-Jimenez, R. Garcia, Identification of single adsorbed cations on mica-liquid interfaces by 3d force microscopy. *J. Phys. Chem. Lett.* **8**, 5707–5711 (2017).
33. Y. G. Chen, J. D. Weeks, Local molecular field theory for effective attractions between like charged objects in systems with strong Coulomb interactions. *Proc. Natl. Acad. Sci. U.S.A.* **103**, 7560–7565 (2006).
34. J. M. Rodgers, J. D. Weeks, Local molecular field theory for the treatment of electrostatics. *J. Phys. Condens. Matter* **20**, 494206 (2008).
35. R. C. Remsing, J. D. Weeks, Hydrophobicity scaling of aqueous interfaces by an electrostatic mapping. *J. Phys. Chem. B* **119**, 9268–9277 (2015).
36. R. C. Remsing, S. Liu, J. D. Weeks, Long-ranged contributions to solvation free energies from theory and short-ranged models. *Proc. Natl. Acad. Sci. U.S.A.* **113**, 2819–2826 (2016).
37. S. Marčelja, N. Radić, Repulsion of interfaces due to boundary water. *Chem. Phys. Lett.* **41**, 129–130 (1976).
38. M. Kanduc, A. Schlaich, E. Schneck, R. R. Netz, "Interactions between biological membranes: Theoretical concepts" in *Soft Interfaces: Lecture Notes of the Les Houches Summer School*, L. Bocquet, D. Quéré, T. A. Witten, L. F. Cugliandolo, Eds. (Oxford University Press, Oxford, United Kingdom, 2017), vol. 98, pp. 385–421.
39. H. Heinz, T. J. Lin, R. K. Mishra, F. S. Emami, Thermodynamically consistent force fields for the assembly of inorganic, organic, and biological nanostructures: The interface force field. *Langmuir* **29**, 1754–1765 (2013).
40. A. Prakash, J. Pfaendtner, J. Chun, C. J. Mundy, Quantifying the molecular-scale aqueous response to the mica surface. *J. Phys. Chem. C* **121**, 18496–18504 (2017).
41. R. T. Cygan, J. J. Liang, A. G. Kalinichev, Molecular models of hydroxide, oxyhydroxide, and clay phases and the development of a general force field. *J. Phys. Chem. B* **108**, 1255–1266 (2004).
42. S. N. Kerisit, J. J. De Yoreo, Effect of hydrophilicity and interfacial water structure on particle attachment. *J. Phys. Chem. C* **124**, 5480–5488 (2020).
43. J. D. Weeks, Connecting local structure to interface formation: A molecular scale van der Waals theory of nonuniform liquids. *Annu. Rev. Phys. Chem.* **53**, 533–562 (2002).
44. J. M. Rodgers, Z. Hu, J. D. Weeks, On the efficient and accurate short-ranged simulations of uniform polar molecular liquids. *Mol. Phys.* **109**, 1195–1211 (2008).
45. J. D. Jackson, "Multipoles, electrostatics of macroscopic media, dielectrics" in *Classical Electrodynamics* (John Wiley & Sons, Hoboken, NJ, 1999), pp. 145–150.
46. C. Zhang, M. Sprik, Electromechanics of the liquid water vapour interface. *Phys. Chem. Chem. Phys.* **22**, 10676–10686 (2020).
47. S. Jin *et al.*, Use of ion exchange to regulate the heterogeneous ice nucleation efficiency of mica. *J. Am. Chem. Soc.* **142**, 17956–17965 (2020).
48. N. N. Lata *et al.*, Multivalent surface cations enhance heterogeneous freezing of water on muscovite mica. *J. Phys. Chem. Lett.* **11**, 8682–8689 (2020).
49. M. Kanduč, A. Schlaich, E. Schneck, R. R. Netz, Hydration repulsion between membranes and polar surfaces: Simulation approaches versus continuum theories. *Adv. Colloid Interface Sci.* **208**, 142–152 (2014).
50. D. Li *et al.*, Trends in mica–mica adhesion reflect the influence of molecular details on long-range dispersion forces underlying aggregation and coalignment. *Proc. Natl. Acad. Sci. U.S.A.* **114**, 7537–7542 (2017).
51. Y. Suzuki *et al.*, Self-assembly of coherently dynamic, auxetic, two-dimensional protein crystals. *Nature* **533**, 369–373 (2016).
52. R. Alberstein, Y. Suzuki, F. Paesani, F. A. Tezcan, Engineering the entropy-driven free-energy landscape of a dynamic nanoporous protein assembly. *Nat. Chem.* **10**, 732–739 (2018).
53. X. Shen, I. C. Bourg, Molecular dynamics simulations of the colloidal interaction between smectite clay nanoparticles in liquid water. *J. Colloid Interface Sci.* **584**, 610–621 (2021).
54. R. M. Pashley, J. N. Israelachvili, Molecular layering of water in thin films between mica surfaces and its relation to hydration forces. *J. Colloid Interface Sci.* **101**, 511–523 (1984).
55. M. L. Sushko, K. M. Rosso, The origin of facet selectivity and alignment in anatase TiO 2 nanoparticles in electrolyte solutions: Implications for oriented attachment in metal oxides. *Nanoscale* **8**, 19714–19725 (2016).
56. A. M. Smith, A. A. Lee, S. Perkin, The electrostatic screening length in concentrated electrolytes increases with concentration. *J. Phys. Chem. Lett.* **7**, 2157–2163 (2016).
57. I. C. Bourg, S. S. Lee, P. Fenter, C. Tournassat, Stern layer structure and energetics at mica–water interfaces. *J. Phys. Chem. C* **121**, 9402–9412 (2017).
58. D. Bodaa, D. Henderson, The effects of deviations from Lorentz-Berthelot rules on the properties of a simple mixture. *Mol. Phys.* **106**, 2367–2370 (2008).
59. I. S. Joung, T. E. Cheatham III, Determination of alkali and halide monovalent ion parameters for use in explicitly solvated biomolecular simulations. *J. Phys. Chem. B* **112**, 9020–9041 (2008).
60. J. Huang, A. D. MacKerell Jr., Charmm36 all-atom additive protein force field: Validation based on comparison to NMR data. *J. Comput. Chem.* **34**, 2135–2145 (2013).
61. J. Yoo, A. Aksimentiev, New tricks for old dogs: Improving the accuracy of biomolecular force fields by pair-specific corrections to non-bonded interactions. *Phys. Chem. Chem. Phys.* **20**, 8432–8449 (2008).
62. M. J. Abraham *et al.*, GROMACS: High performance molecular simulations through multi-level parallelism from laptops to supercomputers. *SoftwareX* **1**, 19–25 (2015).
63. C. Kutzner *et al.*, More bang for your buck: Improved use of GPU nodes for GROMACS 2018. *J. Comput. Chem.* **40**, 2418–2431 (2019).
64. A. Prakash, C. D. Fu, M. Bonomi, J. Pfaendtner, Biasing smarter, not harder, by partitioning collective variables into families in parallel bias metadynamics. *J. Chem. Theor. Comput.* **14**, 4985–4990 (2018).
65. J. Sampath, S. Alamdari, J. Pfaendtner, Closing the gap between modeling and experiments in the self-assembly of biomolecules at interfaces and in solution. *Chem. Mater.* **32**, 8043–8059 (2020).